

Femtosecond Pulse Tailoring For Nanoscale Laser Processing Of Wide-Bandgap Materials: Temporal Asymmetric Pulses Versus Frequency Sweeps

Lars Englert^a, Matthias Wollenhaupt^a, Dirk Otto^a, Cristian Sarpe-Tudoran^a, Alexander Horn^a and Thomas Baumert^a

^a *Institut fuer Physik und CINSaT, Universitaet Kassel, Heinrich-Plett-Str. 40, D-34132 Kassel, Germany (baumert@physik.uni-kassel.de)*

Abstract. Control of two basic ionization processes in dielectrics i.e. photo ionization and electron–electron impact ionization on intrinsic time and intensity scales is investigated experimentally. In our experiment, we use a modified microscope set up to irradiate the surface of a fused silica sample with a single shaped pulse resulting in nanoscale ablation structures. The topology of the laser generated structures is measured by Atomic Force Microscopy (AFM). Structure parameters are investigated as a function of the pulse energy and the modulation parameters. We find different thresholds for surface material modification with respect to an *asymmetric temporal pulse* and its time reversed counterpart both showing a *constant instantaneous frequency*. However, we do not observe pronounced differences between up- and down-chirped radiation (i.e. *symmetric temporal pulse envelope* but *asymmetric instantaneous frequency*) in the measured structure diameters and thresholds.

Keywords: femtosecond pulse shaping, material processing, nanostructuring
PACS: 89.07.-b, 42.65.-k, 42.70.Ce

1. INTRODUCTION

Lasers delivering ultrashort pulses have emerged as a promising tool for processing wide band gap materials for a variety of applications ranging from precision micromachining on and below the wavelength of light to medical surgery [1-3]. Within this context it is the transient free-electron density in the conduction band of the dielectric that plays a fundamental role in addition to various propagation and relaxation mechanisms. A large number of experiments make use of the threshold of observed damage as experimental evidence for exceeding a certain critical electron density (and energy) after the laser interaction. These involve pulse duration measurements [4-6] and recent pulse-train experiments [7] all showing a strong dependence of the damage threshold on pulse duration and on pulse separation. Direct studies of transient electron densities range from intensities below [8,9] up to well above the breakdown threshold. [10,11]. The temporal evolution of the free-electron density and the role of the fundamental ionization processes are strongly depending on time and intensity [12,13]. Two main processes for generating free electrons are multi

photon ionization (MPI) and Avalanche-Ionization (AI). MPI requires no free initial free electrons and has highest efficiency for shortest pulses AI on the other hand needs initial free electrons and needs time to establish.

A “seed” (due to MPI) and “heat” (due to AI) sequence should be an efficient way to achieve the necessary electron density (and energy) for ablation. Two different approaches can be envisioned: Either via temporal asymmetric laser profiles [14,15] or via changing the instantaneous frequency [16]. The first approach can be tested with asymmetric pulses created via Third Order Dispersion (TOD), the second approach via chirped pulses making use of Group Delay Dispersion (GDD).

This contribution is subdivided in two sections: the first part introduces pulse shaping by spectral phase modulation with special emphasis on two exemplary phase functions, i.e. GDD and TOD, leading to symmetric and asymmetric pulse shapes, respectively. In the second section, experimental results on laser ablation at the surface of a fused silica sample with temporally shaped femtosecond laser pulses measured for TOD and GDD are presented.

2. PULSE TAILORING

In this section a brief description of the two pulse shapes that we employ for material processing is given (see. Section 4). We consider two basic pulse shapes to represent more general classes of pulses with different physical properties. The first class of pulses represented by the *linear chirp* is characterized by a *symmetric temporal pulse envelope* $|\mathcal{E}_{\text{mod}}(t)|$, but time varying instantaneous frequency $\omega(t)$. With this class of pulses we study the influence of the time varying instantaneous photon energy $\hbar\omega(t)$ and also the pulse duration on laser processing of wide-bandgap materials. Upon time inversion of this pulse $\mathcal{E}_{\text{mod}}(t) \rightarrow \mathcal{E}_{\text{mod}}(-t)$ the influence of the pulse duration is discriminated from effects due to the time varying photon energy. By contrast, *asymmetric temporal pulse envelopes* featuring a constant instantaneous frequency provide pulses of constant photon energy and variable pulse duration. By time inversion of those pulses the effect of the time-dependent energy flow is identified and allows to address different physical mechanisms of material processing. In our work, asymmetric pulses are generated by Third Order Dispersion (TOD) whereas symmetric pulses are generated by Group Delay Dispersion (GDD).

In order to mathematically describe shaped laser pulses we start by considering an unmodulated bandwidth limited Gaussian pulse envelope

$$\mathcal{E}(t) = \frac{\mathcal{E}_0}{2} e^{-\ln(4)\left(\frac{t}{\Delta t}\right)^2} \quad (1)$$

with a pulse duration of Δt , i.e. the *intensity* Full Width at Half Maximum (FWHM). The complex electric field is described by the product of the envelope function $\mathcal{E}(t)$ and the carrier oscillation at the central laser frequency ω_0

$$E(t) = \mathcal{E}(t) \cdot e^{i\omega_0 t}. \quad (2)$$

The real part of $E(t)$ represents the actual physical electrical field of the laser pulse. Shaped pulses are generated by spectral phase modulation [17,18]

$$\tilde{\mathcal{E}}_{\text{mod}}(\omega) = \tilde{\mathcal{E}}(\omega) \cdot e^{-i\varphi(\omega)}, \quad (3)$$

where $\varphi(\omega)$ denotes the spectral phase modulation function applied to the spectrum $\tilde{\mathcal{E}}(\omega)$ of the pulse. The spectrum $\tilde{\mathcal{E}}(\omega)$ is obtained by *Fourier transform* of the pulse envelope $\mathcal{E}(t)$ whereas the modulated temporal field envelope $\mathcal{E}_{\text{mod}}(t)$ is the *inverse Fourier transform* of the modulated spectrum $\tilde{\mathcal{E}}_{\text{mod}}(\omega)$. Since spectral modulation leaves the Power Spectral Density (PSD) unchanged, i.e. $|\tilde{\mathcal{E}}(\omega)|^2 = |\tilde{\mathcal{E}}_{\text{mod}}(\omega)|^2$, both the PSD of the modulated and the unmodulated spectrum have the same energy bandwidth of

$$\Delta\varepsilon = \hbar\Delta\omega = \hbar \frac{4 \ln(2)}{\Delta t}. \quad (4)$$

Employing common units of meV for the photon energy and fs for the pulse duration one obtains the convenient relation $\Delta\varepsilon [\text{meV}] \approx 1825 / \Delta t [\text{fs}]$.

Group Delay Dispersion (GDD) plays a major role in many applications based on femtosecond pulse manipulation techniques (see for example our own work and references therein [19-22]). GDD is introduced by applying a parabolic spectral phase function

$$\varphi(\omega) = \frac{\phi_2}{2} \cdot \omega^2, \quad (5)$$

to the spectrum $\tilde{\mathcal{E}}(\omega)$ and ϕ_2 is the so-called chirp parameter. A positive value of ϕ_2 leads to an *up-chirped* pulse characterized by an increase of the instantaneous frequency, whereas a negative value of ϕ_2 implies a decrease of the instantaneous frequency, known as *down-chirp*. The modulated pulse envelope is described by

$$\mathcal{E}_{\text{mod}}(t) = \frac{\mathcal{E}_0}{2\gamma^{1/4}} \cdot e^{-\frac{t^2}{4\beta\gamma}} \cdot e^{i(\alpha t^2 - \varepsilon)}, \quad (6)$$

where $\beta = \frac{\Delta t^2}{8 \ln(2)}$ and $\gamma = 1 + \frac{\phi_2^2}{4\beta^2}$ determine the duration of the broadened Gaussian envelope and $\alpha = \frac{\phi_2}{8\beta^2\gamma}$ describes the chirp rate and $\varepsilon = \frac{1}{2} \arctan\left(\frac{\phi_2}{2\beta}\right)$ a temporal phase offset. Figure 1 shows an example of an initially 30 fs FWHM pulse subjected to a Group Delay Dispersion of $\phi_2 = 2500 \text{ fs}^2$ leading to an *up-chirped* pulse. Equation (6) shows that the phase due to the spectral modulation is $\zeta(t) = \alpha t^2 - \varepsilon$ and therefore the time dependent detuning from the central frequency is

$$\Delta(t) = \omega(t) - \omega_0 = \frac{d}{dt} \zeta(t) = 2\alpha t \quad (7)$$

i.e. the instantaneous frequency increases linearly with time, proportional to 2α . This is why GDD is generally referred to as *linear chirp*. However, the chirp rate α is a non-linear function of the chirp parameter ϕ_2

$$\alpha = \left\{ 2\phi_2 + \frac{\Delta t^4}{8\phi_2[\ln(2)]^2} \right\}^{-1}. \quad (8)$$

It takes its maximum value of $\alpha(\phi_2^{\max}) = \frac{\ln(2)}{\Delta t^2}$ at a chirp parameter of $\phi_2^{\max} = \frac{\Delta t^2}{4 \ln(2)}$.

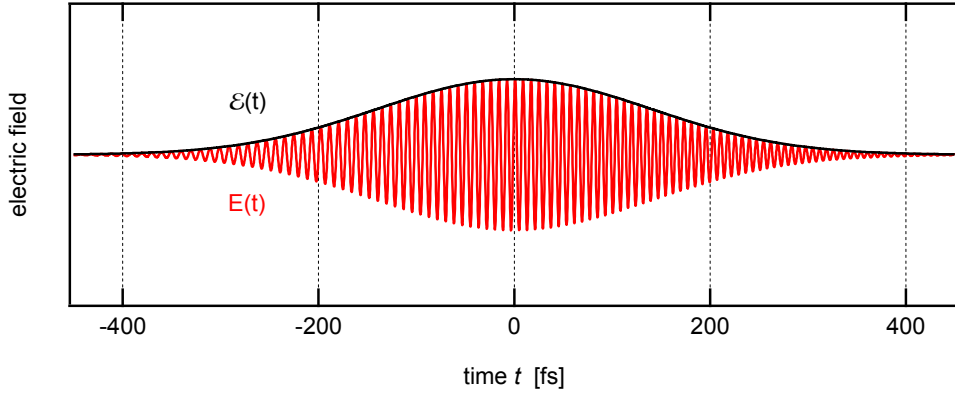


FIGURE 1. Example of a $\Delta t = 30 \text{ fs}$ FWHM pulse subjected to a Group Delay Dispersion of $\phi_2 = 2500 \text{ fs}^2$ leading to an *up-chirped* pulse. In order to visualize the increase of the instantaneous frequency $\omega(t)$ with time the carrier frequency was chosen three times smaller than the actual carrier frequency of $\omega_0 \approx 2.35 \text{ fs}^{-1}$ corresponding to a wavelength of 800 nm. The FWHM of the spectral energy bandwidth is $\Delta\varepsilon = 60.8 \text{ meV}$. The pulse is Gaussian in shape with a pulse duration of 233 fs (FWHM of the intensity).

Since a chirped Gaussian pulse stays Gaussian in shape for any chirp parameter ϕ_2 , we can extract the modulated pulse duration also from Equation (6) by inspection of the denominator in the exponent ($4\beta\gamma$) to obtain the FWHM as

$$\Delta t_{\text{mod}} = \sqrt{\Delta t^2 + 16[\ln(2)]^2 \left(\frac{\phi_2}{\Delta t}\right)^2}. \quad (9)$$

Equation (9) shows that for large values of ϕ_2 , i.e. if $\phi_2 > \Delta t^2$, the pulse duration is predominantly determined by the pulse broadening due to GDD rather than the contribution of the initial pulse duration Δt . In this limit, the pulse duration is linear in the chirp parameter and can be approximated by the simple expression

$$\Delta t_{\text{mod}} = \ln(16) \frac{\phi_2}{\Delta t} \approx 2.77 \frac{\phi_2}{\Delta t}. \quad (10)$$

Since the initial step of the photoelectron generation in wide-bandgap materials is due to multi-photon ionization (MPI) we consider some of the relevant properties of chirped excitation in a multi-photon scenario. In a multi-photon processes involving n photons, the excitation amplitude is proportional to the n^{th} power of the electric field, i.e. $c_n \propto E^n(t)$, provided there are no intermediate resonances available. Hence for a chirped pulse we find the multi-photon field

$$\mathcal{E}_{\text{mod}}^n(t) = \frac{\mathcal{E}_0^n}{2^n \gamma^{n/4}} e^{-n \frac{t^2}{4\beta\gamma}} e^{in(at^2 - \varepsilon)}. \quad (11)$$

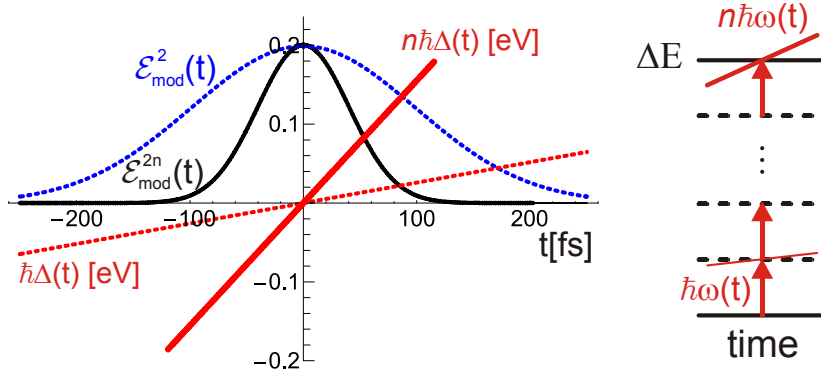


FIGURE 2. Illustration of the multi-photon properties of the up-chirped pulse shown in Fig. 1 for an $n = 6$ photon process. *Left panel:* the *intensity* envelope of the modulated multi-photon field ($\mathcal{E}_{\text{mod}}^{2n}(t)$, black) is much narrower compared to the single photon field ($\mathcal{E}_{\text{mod}}^2(t)$, blue dashed). The time-dependent instantaneous multi-photon energy increases linearly with time ($n\hbar\Delta(t)$, red) - with a slope that is n times steeper than the single photon detuning ($\hbar\Delta(t)$, red dashed). The single-photon energy changes by about 60 meV within $\Delta t_{\text{mod}} = 233$ fs (FWHM of the single-photon field) whereas the multi-photon energy changes by about 148 meV within a time interval of $\Delta t_{\text{mod}} / \sqrt{n} = 95$ fs (FWHM of the single-photon field). *Right panel:* due to the multi-photon chirp the time-dependent multi-photon energy $n\hbar\omega(t)$ may cross the bandgap ΔE during the interaction. In general, a frequency sweep addresses different densities of states as a function of the instantaneous frequency.

Because the field is proportional to a high power of the modulated single photon field envelope $\mathcal{E}_{\text{mod}}(t)$, the envelope of the modulated multi-photon field $\mathcal{E}_{\text{mod}}''(t)$ is much narrower compared to the single photon field (see Fig. 2 for a comparison of the respective *intensity* envelopes $\mathcal{E}_{\text{mod}}^{2n}(t)$ and $\mathcal{E}_{\text{mod}}^2(t)$). In fact, it follows from Equation (11) that the (intensity) FWHM of the modulated field reduces by a factor of \sqrt{n} . Equation (11) also shows that the effective instantaneous frequency of the multi-photon field increases linearly with time proportional to $2n\alpha$

$$\omega_n(t) = n\omega_0 + 2n\alpha t, \quad (12)$$

with a slope that is n times steeper than the single photon detuning $\hbar\Delta(t)$ (cf. Equation (7)) as illustrated on the left panel of Fig. 2. For example, the *single-photon* energy of a chirped pulse (GDD of $\phi_2 = 2500 \text{ fs}^2$, initially $\Delta t = 30 \text{ fs}^2$ as shown in Fig. 1) changes by about $\delta\varepsilon = 2\hbar\alpha\Delta t_{\text{mod}} \approx 60 \text{ meV}$ within the FWHM of the single-photon field of $\Delta t_{\text{mod}} = 233 \text{ fs}$. In contrast, the *multi-photon* energy changes by about $2n\hbar\alpha\Delta t_{\text{mod}} / \sqrt{n} = \sqrt{n}\delta\varepsilon \approx 148 \text{ meV}$ within the FWHM of the multi-photon field $\Delta t_{\text{mod}} / \sqrt{n} = 95 \text{ fs}$ as shown in the left panel of Fig. 2. Because of this chirp, the time-dependent multi-photon energy $n\hbar\omega(t)$ may cross the band gap ΔE during the interaction (see Fig. 2). Therefore, one could assume that the properties of laser generated nano-structures are controllable by the temporal direction of the chirp as suggested by Louzon et al. [16]. This reasoning also motivates our investigations of the diameters of nano-structures produced by chirped laser pulses as a function of the chirp parameter presented in Section 4.

Third Order Dispersion (TOD) introduced via a cubic spectral phase function

$$\varphi(\omega) = \frac{\phi_3}{6} \cdot \omega^3 \quad (13)$$

leads to a modulated pulse shape that is characterized by an intense initial pulse followed by a pulse sequence with decaying amplitudes [23]. An example of a 30 fs FWHM pulse subjected to TOD with $\phi_3 = 90000 \text{ fs}^3$ is depicted in Fig. 3. In sharp contrast to quadratic spectral phase modulation, applying the cubic phase function results in shaped pulse with *constant instantaneous* frequency. Since antisymmetric spectral phase functions always give rise to real valued pulse envelopes, the temporal phase is zero at all times, and, hence the instantaneous frequency $\omega(t) = \omega_0$ is constant throughout the shaped pulse. The sign of ϕ_3 controls the temporal direction of the pulse shape: positive values of ϕ_3 lead to a series of post-pulses (as depicted in Fig. 3) whereas negative values of ϕ_3 result in a series of pre-pulses.

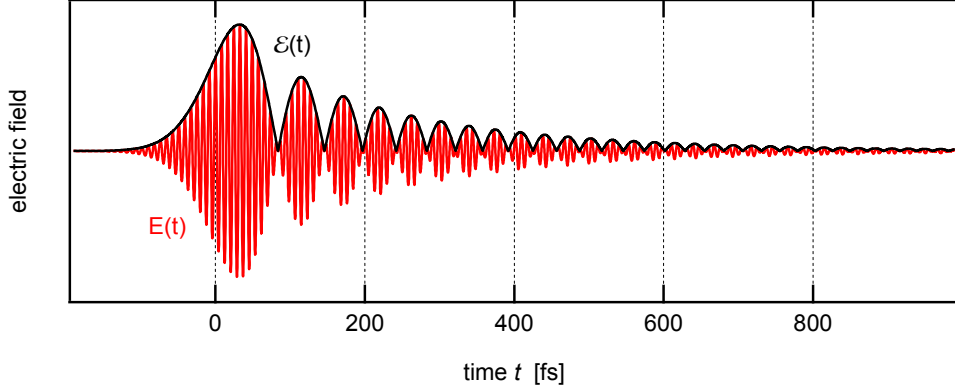


FIGURE 3. Example of a $\Delta t = 30$ fs FWHM pulse subjected to Third Order Dispersion (TOD) of $\phi_3 = 90000$ fs³. The pulse starts with an intense sub-pulse followed by a long pulse train. The statistical pulse duration $\Delta t = \sqrt{8 \ln(2)} \sigma_t$ is 233 fs like in the GDD example in Fig. 1. For visualization purposes, the carrier frequency was chosen three times smaller than the actual carrier frequency (see above).

Since TOD pulses are asymmetrically broadened in time, the temporal FWHM is no longer a unique quantity to describe the pulse duration. Therefore, we use the *statistical pulse duration* σ_t to describe the pulse duration [23]. Since the statistical pulse duration delivers shorter values for an unmodulated Gaussian pulse compared to the FWHM, we define the modulated pulse duration by $\Delta t_{mod} = \sqrt{8 \ln(2)} \sigma_t$ to obtain a quantitative measure of the pulse duration

$$\Delta t_{mod} = \sqrt{\Delta t^2 + 16 [\ln(2)]^3 \left(\frac{\phi_3}{\Delta t^2} \right)^2}, \quad (14)$$

that agrees with the FWHM for the unmodulated pulse. Equation (14) shows that in case of TOD – in the same manner as for GGD – for large values of ϕ_3 , i.e. if $\phi_3 > \Delta t^3$, the pulse duration is linear in the TOD parameter ϕ_3 and can be approximated by the simple expression

$$\Delta t_{mod} \approx 4 [\ln(2)]^{3/2} \frac{\phi_3}{\Delta t^2} \approx 2.31 \frac{\phi_3}{\Delta t^2}. \quad (15)$$

With respect to nanoscale laser processing of wide-band-gap materials the relevant features of TOD are the temporal symmetry-breaking of the envelope implying control on the time-dependent energy flux onto the sample and, in particular, the ability to produce a short intense pre-pulse accompanied by a weak long pulse train. In Section 4 we will use TOD spectral modulation to exert control on two basic ionization processes to manipulate the ablation dynamics.

3. EXPERIMENTAL SET UP

In this section we give a brief description of our experimental set up shown schematically in the left panel of Fig. 4. In our experiment we combine spectral femtosecond pulse shaping techniques with a microscope set up for nanoscale laser processing. Laser radiation with 35 fs (FWHM) pulse duration and a central wavelength of 790 nm is provided by an amplified Ti:Sapphire laser system (Femtolasers Femtopower Pro). Temporal shaping of the laser radiation is achieved by a home-built spectral phase modulator [24]. The radiation is focused via a Zeiss Epiplan 50x/0.5NA objective to a spot with a calculated lateral diameter of 1.4 μm (using a $1/e^2$ intensity profile of the point spread function [25]). The calculated axial spot size in air is 9.1 μm . Structures are generated irradiating the surface of fused silica with one pulse followed by ablation. The smallest pulse duration in the interaction region is obtained by adjusting the prism compressor in the amplified Ti:Sapphire laser system pre-compensating the dispersion of the optical elements in the subsequent beam path. Temporal pulse characterization is achieved by 2nd order auto-correlation and cross-correlation using a Mach-Zehnder interferometer in the beam path and detecting the resulting radiation by a 2-photon photodiode after the focusing objective. Applying a cubic phase mask on the phase modulator results in an asymmetric pulse in time domain exemplified by the cross-correlation trace between the unshaped and the shaped pulse as shown in the right panel of Fig. 4.

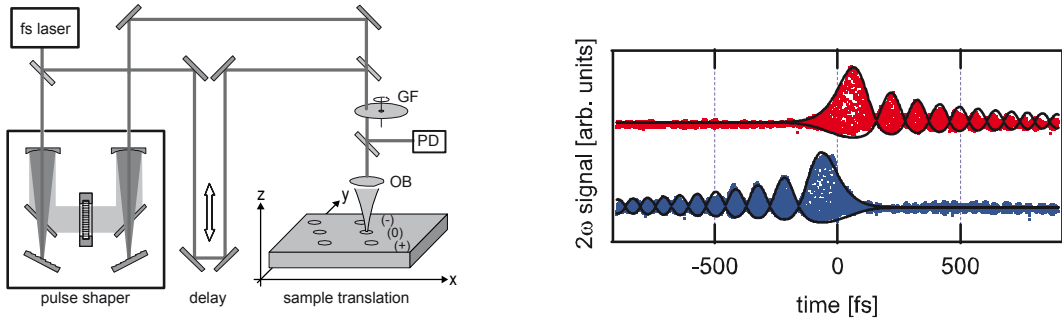


FIGURE 4. *Left:* The experimental setup. The femtosecond laser beam is aligned into the spectral phase modulator. Energy is controlled by a motorized neutral density gradient filter (GF) and monitored with a photodiode (PD). A microscope objective (OB) focuses the beam on the dielectric sample. Sample translation is done by a 3-axis piezo table. *Right:* Measured (dots) and simulated (solid lines) cross-correlations for a cubic phase mask of $\phi_3 = +6 \times 10^5 \text{ fs}^3$ (top) and $\phi_3 = -6 \times 10^5 \text{ fs}^3$ (bottom).

The fused silica sample (Heraeus Suprasil) was cleaned prior and after material processing using an alkaline (KOH solved in isopropanol) and dilute hydrochloric acid solutions in a supersonic bath. For material processing shaped femtosecond laser radiation is focused onto the sample surface. The single shot pulse energy is adjusted by a motor driven gradient neutral density filter and recorded with a photodiode. The photodiode was calibrated with a commercial power meter. The sample is translated by a 3-axis piezo table to a new sample position for each shot. Reproducible z-positioning is assured by confocal probing of the sample surface with cw-HeNe laser radiation prior to material processing. The spectral phase mask, energy and focal z-

position are varied. Energy threshold values and structure sizes are obtained from the topology of the atomic force microscopy (AFM) measurements.

4. RESULTS AND DISCUSSION

In recent experiments [14,15] we studied material processing of dielectrics with temporally asymmetric femtosecond laser pulses generated by TOD. In that work, shaped laser pulses were employed to generate structures one order of magnitude smaller in diameter than those produced by unshaped radiation at the same energy. In addition, different thresholds for surface material modification were observed for modulated pulses and their time reversed counterparts. The thresholds for material damage were determined by visual inspection from scanning electron microscopy (SEM) micrographs.

In this work, we investigate ablated structures generated by TOD pulses with $\phi_3 = \pm 6 \times 10^5 \text{ fs}^3$ resulting in a statistical pulse duration of $\Delta t_{mod} \approx 1 \text{ ps}$ (see Section 2). In addition to our earlier studies [14,15], diameters and depths of the structures are extracted from their topology measured by AFM. A comparison of the results from both measurement techniques SEM and AFM is depicted in Fig. 5.

Here, the *inner diameter* determined by AFM is defined by the diameter at which the height profile falls below the unperturbed surface level (see blue arrows in the section through the AFM micrograph in Fig. 5). The maximum depth of the generated structures has been measured by AFM to 750 nm and may be limited by the shape of the used high aspect ratio tip. The shape of the high aspect ratio tip is also responsible for the asymmetry in profile. The detailed information on the topography of the structures available by AFM allows us to map the locus of maximum contrast in the SEM micrographs to the regions of maximum slope due to the high aspect ratio of the hole (see red arrows in the section through the AFM micrograph in Fig. 5). As a consequence, the *inner diameter* for a given structure takes a slightly larger value compared to the diameter obtained solely by the region of highest contrast in the SEM micrograph as used in our previous publications. This region, i.e. the deep channel diameter, stays remarkably stable with respect to energy variations [14,15].

The hole diameters of ablated structures for fused silica with $\phi_3 = +6 \times 10^5 \text{ fs}^3$ (red triangles) and $\phi_3 = -6 \times 10^5 \text{ fs}^3$ (blue triangles) measured by AFM are shown on the left side of Fig. 6. By modulating laser radiation with TOD $\phi_3 = \pm 6 \times 10^5 \text{ fs}^3$ a reduction up to an order of magnitude (below the diffraction limit) in the structure diameter (as small as 100 nm) is observed. For the negative cubic phase ($-6 \times 10^5 \text{ fs}^3$) the threshold for material processing is larger than for the positive cubic phase, while the structure size is also well below the diffraction limit. As the pulses feature identical fluence, spectrum and pulse duration it is the different asymmetric temporal shape, i.e. the energy distribution in time that has a significant influence on the material damage threshold.

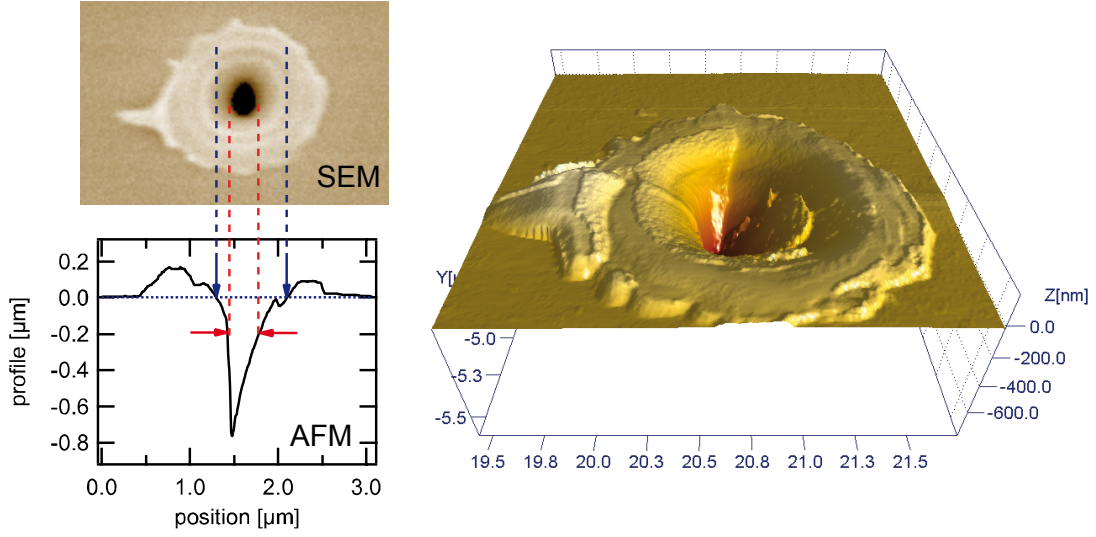


FIGURE 5. *Left:* SEM micrographs of a structure generated by positive TOD radiation with pulse energy twice above the threshold at $\phi_3 = +6 \times 10^5 \text{ fs}^3$. The corresponding depth profile measured by AFM is shown below. In this publication the term inner diameter relate to the diameter where the height profile falls below the unperturbed surface level (blue arrows). Note that the clearly visible contrast change in the SEM micrograph results from the high aspect ratio of the hole (red arrows). This deep channel diameter stays remarkably stable with respect to energy variations. [14,15] *Right:* AFM micrograph corresponding to the SEM micrograph shown left.

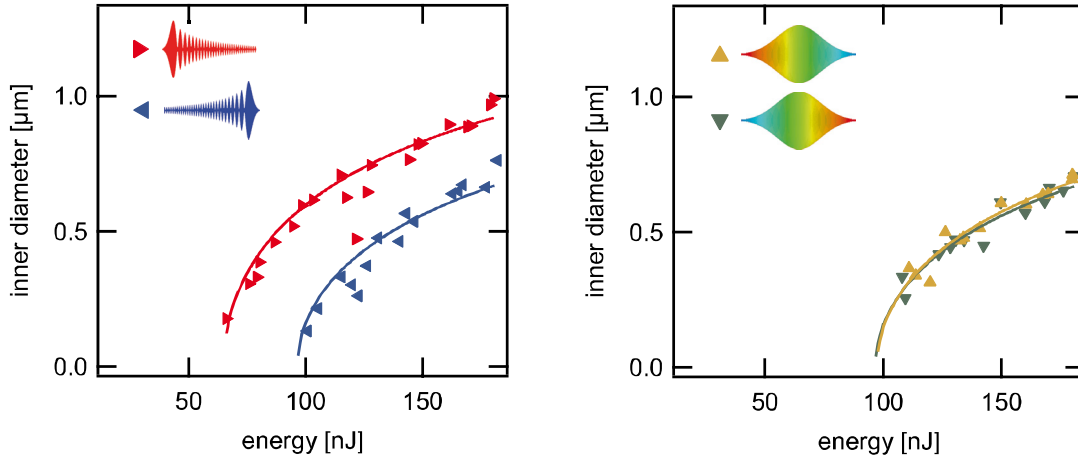


FIGURE 6. *Left:* (TOD) inner hole diameters of ablated structures for fused silica with $\phi_3 = +6 \times 10^5 \text{ fs}^3$ (red triangles) and $\phi_3 = -6 \times 10^5 \text{ fs}^3$ (blue triangles) measured by AFM. *Right:* (GDD) inner hole diameters of ablated structures for fused silica with $\phi_2 = +1 \times 10^4 \text{ fs}^2$ (orange triangles) and $\phi_2 = -1 \times 10^4 \text{ fs}^2$ (green triangles) measured by AFM.

The threshold energies for ablation were determined by fitting the observed energy dependent hole diameters $d(E)$ to the relation [26]

$$d(E) \propto \sqrt{\ln(E)} \quad (16)$$

In contrast to reported structure diameters of below 100 nm and occasionally up to 15nm created at the backside of the substrate using high NA immersion objectives [27] and additionally in conjunction with super resolving pupil plane filters [28] our method works with a long-distance air objective directly on the surface side of the substrate.

The physics of the ablation process induced by TOD spectral phase modulated pulses has been discussed in terms of a '*seed and heat*' mechanism for electrons [14,15], where reaching a critical electron density (and energy) is generally attributed to the threshold for laser ablation. Especially the interplay of the two main processes for generating free electrons by multi photon-Ionization (MPI) and Avalanche-Ionization (AI) permitted to exert control on the ablation process as mentioned in the introduction. MPI requires no free initial free electrons and has highest efficiency for shortest pulses with highest intensities. AI, on the other hand, needs initial free electrons and needs time to establish. When distributing the intensity from the main pulse to some consecutive pulses, the amount of free electrons created by the first strong sub-pulse via MPI is not sufficient for reaching the critical electron density. However, the consecutive pulses can increase the electron density via AI to the critical density. For $\phi_3 < 0$, the intensity of the pulses increases and is terminated by a strong pulse. The first weak pulses are not intense enough for efficient MPI, and due to the absence of free electrons, also an increase of the free electron density due to AI is not operative. Only the final sub-pulse(s) is (are) able to deliver free electrons via MPI further increased by AI during the trailing part of the pulse. For this case, a higher energy is needed in comparison to $\phi_3 > 0$ in order to reach the critical density. In this sense, we exert control on the two ionization processes by employing temporally asymmetric pulse shapes.

A similar physical mechanism was proposed to be at play for laser processing of wide-bandgap materials with chirped laser pulses [16]. Because the temporal intensity profile $|\mathcal{E}_{mod}(t)|^2$ of a chirped pulse is always symmetric $|\mathcal{E}_{mod}(t)|^2 = |\mathcal{E}_{mod}(-t)|^2$ the "seed and heat" mechanism was assumed to be operative due to the linear energy sweep in a chirped pulse, i.e. the time dependent multi-photon energy described in Section 2. Since the blue spectral components arrive before the red spectral components in a *down-chirped* pulse, the early blue spectral components may have sufficient energy to overcome the multi-photon energy threshold to provide the initial "seed" electrons in the conduction band. Those electrons would be "heated" during the trailing edge of the pulse. In contrast, an up-chirped pulse—starting with lower energy red spectral components—might, for a given number of photons, not overcome the required multi-photon energy threshold. Alternatively, a higher-order multi-photon process is required for the generation of electrons in the conduction band. In general, a frequency sweep addresses different density of states as a function of the instantaneous frequency. In all cases, either no or a lower number of initial seed electrons is expected for up-chirped laser pulses resulting in no effective "heating" which should lead to a higher threshold for ablation.

In order to reinvestigate the effect of the temporal asymmetry in the instantaneous frequency under our experimental conditions, we studied ablation with chirped pulses

for $\phi_2 = \pm 1 \times 10^4 \text{ fs}^2$ resulting in a pulse duration of $\Delta t_{\text{mod}} \approx 0.8 \text{ ps}$ (cf. Equation (9) in Section 2). The right side of Fig. 6 shows the observed diameters of the ablated structures for fused silica with *up-chirped* ($\phi_2 = +1 \times 10^4 \text{ fs}^2$, orange triangles) and *down-chirped* ($\phi_2 = -1 \times 10^4 \text{ fs}^2$, green triangles) pulses as measured by AFM. Although Louzon et al. [16] reported an up to 20% threshold fluence reduction for *down-chirped* pulses, we do not observe pronounced differences between up- and down-chirped radiation in the measured structure diameters indicated by the overlap of both the fitted orange and green curves through the measured data. Note that the minimal structure sizes obtained with TOD pulses are smaller as compared to those obtained by GGD pulses.

5. CONCLUSION

In this contribution we have investigated single shot nanoscale laser processing of a wide-bandgap material (fused silica) with two classes of temporally shaped femtosecond laser pulses. Temporal shaping was achieved by spectral phase modulation, where *asymmetric temporal pulse envelopes with constant instantaneous frequency* were generated by Third Order Dispersion (TOD) and *symmetric temporal pulse envelopes with frequency sweeps* were generated by Group Delay Dispersion (GDD).

In the experiment, we studied the topology of laser generated structures for both classes of pulses by Atomic Force Microscopy (AFM) as a function of the pulse energy and the modulation parameters. Our results showed different thresholds for surface material modification with respect to an asymmetric pulse and its time reversed counterpart. The physical mechanism of the ablation process induced by the asymmetric pulses was discussed in terms of a '*seed and heat*' model for electrons, i.e. the interplay of the two main processes for generating free electrons by Multi Photon-Ionization (MPI) and Avalanche-Ionization (AI). Control by asymmetric pulse shapes is exerted because the direct temporal profile and its time inverted profile address the two ionization processes in a different fashion. In contrast to our findings for asymmetric pulses, for symmetrical pulses we do not observe pronounced differences in the measured structure diameters upon up- and down-chirped radiation. In addition, we found that the minimal structure sizes obtained with TOD pulses are smaller as compared to those obtained by GGD pulses.

We conclude that control of ionization processes with tailored femtosecond pulses, and in particular strongly temporal asymmetric pulse shapes, opens the route to develop optimal pulse shapes for controlled nanoscale material processing of dielectrics.

ACKNOWLEDGMENTS

We gratefully acknowledge financial support by the Deutsche Forschungsgemeinschaft DFG and the European Commission project FASTQUAST.

REFERENCES

1. H. Misawa and S. Juodkazis, *3 D Laser Microfabrication* (WILEY-VCH Verlag GmbH & Co. KGaA, 2006).
2. A. Vogel, J. Noack, G. Hüttman, and G. Paltauf, *Appl. Phys. B* **81**, pp. 1015-1047 (2005).
3. M. Wollenhaupt, L. Englert, A. Horn, and T. Baumert, *J. Laser. Micro. Nano.* **4**, pp. 144-151 (2009).
4. A. C. Tien, S. Backus, H. C. Kapteyn, M. M. Murnane, and G. Mourou, *Phys. Rev. Lett.* **82**, pp. 3883-3886 (1999).
5. M. Lenzner, J. Krüger, S. Sartania, Z. Cheng, Ch. Spielmann, G. Mourou, W. Kautek, and F. Krausz, *Phys. Rev. Lett.* **80**, pp. 4076-4079 (1998).
6. B. C. Stuart, M. D. Feit, A. M. Rubenchik, B. W. Shore, and M. D. Perry, *Phys. Rev. Lett.* **74**, pp. 2248-2251 (1995).
7. R. Stoian, M. Boyle, A. Thoss, A. Rosenfeld, G. Korn, and I. V. Hertel, *Appl. Phys. A* **77**, pp. 265-269 (2003).
8. V. V. Temnov, K. Sokolowski-Tinten, P. Zhou, A. El-Khamhawy, and D. von der Linde, *Phys. Rev. Lett.* **97**, pp. 237403-237403-4 (2006).
9. S. S. Mao, F. Quéré, S. Guizard, X. Mao, R. E. Russo, G. Petite, and P. Martin, *Appl. Phys. A* **79**, pp. 1695-1709 (2004).
10. C. Sarpe-Tudoran, A. Assion, M. Wollenhaupt, M. Winter, and T. Baumert, *Appl. Phys. Lett.* **88**, pp. 261109-261109-3 (2006).
11. I. H. Chowdhury, X. Xu, and A. M. Weiner, *Appl. Phys. Lett.* **86**, pp. 151110-151110-3 (2005).
12. A. Kaiser, B. Rethfeld, M. Vicanek, and G. Simon, *Phys. Rev. B* **61**, pp. 11437-11450 (2000).
13. B. Rethfeld, *Phys. Rev. Lett.* **92**, pp. 187401-1-187401-4 (2004).
14. L. Englert, B. Rethfeld, L. Haag, M. Wollenhaupt, C. Sarpe-Tudoran, and T. Baumert, *Optics Express* **15**, pp. 17855-17862 (2007).
15. L. Englert, M. Wollenhaupt, L. Haag, C. Sarpe-Tudoran, B. Rethfeld, and T. Baumert, *Appl. Phys. A* **92**, pp. 749-753 (2008).
16. E. Louzon, Z. Henis, S. Pecker, Y. Ehrlich, D. Fisher, M. Fraenkel, and A. Zigler, *Appl. Phys. Lett.* **87**, pp. 241903-241903-3 (2005).
17. A. M. Weiner, *Rev. Sci. Instr.* **71**, pp. 1929-1960 (2000).
18. M. Wollenhaupt, A. Assion, and T. Baumert, "Femtosecond Laser Pulses: Linear Properties, Manipulation, Generation and Measurement" in *Springer Handbook of Lasers and Optics*, F. Träger, ed. (Springer Science + Business Media, New York 2007).
19. M. Wollenhaupt, V. Engel, and T. Baumert, *Ann. Rev. Phys. Chem.* **56**, pp. 25-56 (2005).
20. M. Wollenhaupt, A. Präkelt, C. Sarpe-Tudoran, D. Liese, and T. Baumert, *Appl. Phys. B* **82**, pp. 183-188 (2006).
21. M. Krug, T. Bayer, M. Wollenhaupt, C. Sarpe-Tudoran, T. Baumert, S. S. Ivanov, and N. V. Vitanov, *New J. Phys.* **11**, pp. 105051 (2009).
22. A. Assion, T. Baumert, J. Helbing, V. Seyfried, and G. Gerber, *Chem. Phys. Lett.* **259**, pp. 488-494 (1996).
23. M. Wollenhaupt, A. Assion, and T. Baumert, in *Springer Handbook of Lasers and Optics*, F. Träger, ed. (Springer Science and Business Media, 2007).
24. A. Präkelt, M. Wollenhaupt, A. Assion, C. Horn, C. Sarpe-Tudoran, M. Winter, and T. Baumert, *Rev. Sci. Instr.* **74**, pp. 4950-4953 (2003).
25. M. Martinez-Corral, "Point spread function engineering in confocal scanning microscopy" in *Wave-Optical Systems Engineering II, Proceedings of SPIE*, F. Wyrowski, ed. (2003).
26. J. M. Liu, *Opt. Lett.* **7**, pp. 196-198 (1982).
27. A. P. Joglekar, H. Liu, G. J. Spooner, E. Meyhöfer, G. Mourou, and A. J. Hunt, *Appl. Phys. B* **77**, pp. 25-30 (2003).
28. M. Merano, G. Boyer, A. Trisorio, G. Chériaux, and G. Mourou, *Opt. Lett.* **32**, pp. 2239-2241 (2007).